Comprehensive study of WSiC:H coatings synthesized by microwave-assisted RF reactive sputtering

Aissatou Diop, Danielle Ngoue, Amine Mahammou, Babacar Diallo, Béatrice Plujat, Angélique Bousquet, Thierry Sauvage, Sébastien Quoizola, Mireille Richard-Plouet, Jonathan Hamon, et al.

Comprehensive study of WSiC:H coatings synthesized by microwave-assisted RF reactive sputtering

Aissatou Diop [1,2], Danielle Ngoue [1,2], Amine Mahammou [1,2], Babacar Diallo [3], Béatrice Plujat [1,2], Angélique Bousquet [4], Thierry Sauvage [3], Sébastien Quoizola [1,2], Mireille Richard-Plouet[5], Jonathan Hamon[5], Audrey Soum-Glaude [1*], Éric Tomasella [4], Laurent Thomas [1,2]

[1] PROMES-CNRS UPR 8521 (Laboratory of PROcess, Materials, Solar Energy), Rambla de la Thermodynamique 66100 Perpignan, France / 7 rue du Four Solaire 66120 Font-Romeu-Odeillo-Via, France

[2] Université de Perpignan Via Domitia, 52 Avenue Paul Alduy 66860 Perpignan, France

[3] CEMHTI-CNRS UPR 3079 (Conditions Extrêmes et Matériaux : Haute Température et Irradiation), Université d'Orleans, Site Cyclotron, 3A rue de la Férollerie 45071 Orléans, France

[4] Université Clermont Auvergne, CNRS, SIGMA Clermont, ICCF, 24 Avenue Blaise Pascal 63178 Aubière, France

[5] Nantes Université, CNRS, Institut des Matériaux de Nantes Jean Rouxel, IMN, F-44000 Nantes, France

[*] Corresponding author - E-mail address: Audrey.Soum-Glaude@promes.cnrs.fr

ABSTRACT

WSiC:H coatings were elaborated by reactive magnetron sputtering of a W target in an $Ar/Si(CH_3)_4$ plasma assisted by ECR microwave sources. Such coatings can be very interesting for optical or mechanical applications. The development of these coatings is based on the confrontation between in-situ diagnostics of the reactive plasma phase and material characterization of the resulting coatings. The investigation by optical emission spectroscopy of the different phenomena occurring in the reactive plasma reveals that there is a precursor flow rate range where W particles can be favored in the reactive plasma, to promote the development of composite coatings based on a SiC:H matrix, in which W-containing particles or aggregates are present. Material characterization such as Scanning Electron Microscopy, Ion Beam Analysis and X-ray Photoelectron Spectroscopy are used to study the impact of the plasma phase on the microstructure and chemical composition of the deposited materials.

Keywords: Plasma processes; Optical Emission Spectroscopy; Thin films; Ion Beam Analysis.

1. INTRODUCTION

Ceramic-metal composites or cermets are known for their advantages such as resistance to corrosion and oxidation [1–3] but also for their disadvantages such as brittleness and the random nature of their cracking. This cracking depends essentially on the nature of the metallic phases inserted in the ceramic matrix. [4,5] They have also attracted a lot of interest in the thermodynamic conversion of solar energy because of their suitable optical properties. Indeed, inserted in a multilayer stack with a metallic lower layer and an antireflective top layer, their solar absorptance can reach 0.94 and their thermal emittance 0.07 as shown by Sathiaraj et al. [6]. However, cermets also have low thermal resistance, especially in air, especially when the nanometric particles included in the matrix are noble metals [7] as opposed to metals such as molybdenum and cobalt.[8,9]. On the subject of thermal stability, $Pt - Al_2O_3$ cermet was found to be stable up to 600°C. [8,10] Antonaia et al also showed that $W - Al_2O_3$ cermet was thermally stable after annealing at 580°C. [11] In this perspective, nanocomposite cermets of the W-SiCH type could be one of the solutions to this problem since the materials used are known to be resistant and stable at high temperatures.[12,13] Indeed, silicon carbide is an ultra-refractory ceramic due to its thermal stability which can go beyond 2000°C [14] and has good oxidation and corrosion resistance after the formation of a silica (SiO_x) passivation layer on its surface. Also, Tungsten is a refractory transition metal with good heat and electrical conductivity. A protective oxide layer is formed on its surface when exposed to air above 400°C. [15,16], Tungsten (melting point of 3420°C) is resistant to corrosion and other various chemical attacks to which it may be exposed.

There are many possible ways to elaborate cermet coatings, depending on the application for with these materials are going to be used.[17–20] In this work, we investigate the possibility of synthesizing WSiC:H coatings by reactive radio frequency (RF) magnetron sputtering [21–23] of a tungsten target in an Ar plasma, in the presence of TetraMethylSilane (TMS: $Si(CH_3)_4$) gaseous precursor. The dissociation of the TMS precursor is assisted by microwave Electron Cyclotron Resonance (ECR) sources. The particularity of this process, which is nevertheless versatile [24], resides in the presence of the reactive plasma phase during the sputtering of the metallic target, leading to the formation of metallic inclusions in a ceramic matrix. This works aims at a better understanding of the links between the plasma deposition process and the microstructure of the resulting films, to better control the latter. For this purpose, non-intrusive optical emission spectroscopy (OES) was implemented to identify the different emitting species occurring in the plasma phase, in order to optimize the coatings deposition process by correlating the species responsible for their growth with the chemical properties of the resulting films. To do so, the physicochemical properties of the latter were thoroughly studied thanks to SEM (Scanning Electron

Microscopy), EDS (Energy Dispersive X-ray Spectrometry), IBA (Ion Beam Analysis) techniques including RBS (Rutherford Back Scattering Spectroscopy), NRA (Nuclear Reaction Analysis) and ERDA (Elastic Recoil Detection Analysis) and X-ray Photoelectron Spectroscopy (XPS).

2. EXPERIMENTAL DETAILS

2.1. Coating synthesis

The materials were developed in the IDEFIX vacuum reactor designed at PROMES-CNRS laboratory [25]. It consists in a cylindrical enclosure on which are placed four coaxial microwave sources of dipolar type (with magnet) which are maintained by water-cooled flanges and connected to a SAIREM GMP16KTS microwave generator operating at 2.45 GHz, which supplies them with a maximum power of 250 W each. It also comprises a heated substrate holder (up to 600°C), a magnetron sputtering cathode (connected to a Caesar RF generator supplied by Advanced Energy operating at a frequency of 13.56 MHz) and is connected to a pumping system (a primary roots pump from Alcatel Adixen to achieve a pressure of around 10^{-2} mbar and secondary turbomolecular pump from Edwards to achieve a vacuum of down to 10^{-6} mbar). The flanges allow the reactor to be used in two different configurations: a cylindrical configuration for deposition on cylindrical substrates and a planar configuration, which was used in this study to deposit on planar samples.

A W underlayer was deposited by RF magnetron sputtering (referred to as Physical Vapor Deposition, PVD in the following) of a solid W target in 20 sccm of Ar gas during 4.5 min. Depending on the final application, this underlayer can be used as an infrared reflector, as a substrate protector or simply as a layer to avoid the effect of the substrate [12]. The distance between the substrate and the target was set at 8.5 cm. For the WSiC:H coatings, a dual process was used: the SiC:H ceramic phase was provided by the plasma decomposition of the gaseous precursor TetraMethylSilane TMS ($Si(CH_3)_4$) diluted in Ar (Plasma Enhanced Chemical Vapor Deposition, PECVD), while the W metallic phase was provided by RF magnetron sputtering. This dual process is assisted by a microwave power of 850 W supplied by the ECR sources distributed coaxially at mid-height of the reactor. The total gas flow rate in the reactor for each deposition is 25 sccm (Ar + TMS) corresponding to a working pressure of 0.1 Pa (10^{-3} mbar). The deposition duration is fixed at 10 min. The two layers of the coatings were deposited consecutively in the same run, without exposure to air.

For more flexibility in the characterizations, especially for those that require slicing the material, the coatings were deposited on silicon wafers (diameter 50.9 +/- 0.3 mm and thickness 280 +/-25 µm, P-doped, N-type, resistivity 1-10 Ωcm, both sides polished) and T91 steel wafers (diameter 1 and 2 inches,

polished on one side). The substrates were in-situ cleaned by an argon plasma generated by a LF-5 RFPP low frequency generator with an Ar flow rate of 50 sccm, and then heated at 350°C for 30 min

2.2. Characterization techniques

2.2.1. Optical emission spectroscopy (OES)

OES is a plasma characterization technique that allows the detection of different emissive species present in the plasma and their quantification without disturbing the plasma. This can be done in the plasma volume but also close to the surface of the growing film, which can give indications on the species sputtered or re-emitted by the surface.

To carry out the spectroscopic measurements, a quartz window (wide spectral range of optical transmission) was installed on the reactor. The experimental set-up for the acquisition consisted of three main parts:

- The optical fiber that guides the light from the source to the spectrophotometer. It is fitted at the end with a lens and a diaphragm for optical sighting, which is itself fixed on a plate. In this study, the aiming point of the fiber is located close to the surface of the substrate and at equidistance from the microwave sources;
- The AvaSpec spectrophotometer [26] from Avantes, which separates the lines brought back by the fiber as a function of wavelength thanks to a mirror and diffraction grating system. It can acquire spectra in the 200-1100 nm range;
- The acquisition system: the spectrophotometer is connected to a computer which allows the acquisition and processing of data using the Avasoft software.[27]

To determine the relative (or normalized) intensities ($I_{r(X)}$) of the monitored species, we use a normalization technique called actinometry demonstrated by Equation (1). It consists in the ratio between the raw emission intensity ($I_{(X)}$) of each peak of the spectra acquired and the product of the integration time t of the system and the emission intensity of the argon line (I_{Ar}) at 696 nm called actinometer.

$$I_{r(X)} = I_{(X)}/(t * I_{Ar}) \quad (1)$$

OES characterization also allowed estimation of the electron temperature (T_e) which corresponds to the mean energy of the electrons present in the plasma phase expressed in eV and given by equation (2).[28]

$$T_e = \frac{hc}{k}(E_m - E_p)/ln\left(\frac{I_{pn}A_{ms}g_{ms}\upsilon_{ms}}{I_{ms}A_{pn}g_p\upsilon_{pn}}\right) \quad (2)$$

Where g and A are respectively the static weights of the energy levels and the probabilities of transitions, h is Planck's constant, k is Boltzmann's constant and c is the speed of light. We use the values of theses

parameters mentioned in Table 1. This temperature actually corresponds to the average temperature of the electrons in the case of a distribution of their energy according to a Maxwell-type distribution function.[29]

Table 1: Values of the constants used for the calculation of the electron temperature

Constants	*m → s (Ar transition)*	*p → n (Ar transition)*
Wavelength (λ) (nm)	702.19	706.16
Frequency (v) (s^{-1})	$4.27503 * 10^{14}$	$4.25098 * 10^{14}$
Einstein's coefficients (A) (s^{-1})	2670000	3800000
Energie (E) (m^{-1})	11968303	10728970
Static weight (g)	5	
Planck's constant (h) (J.s)	$6.62 * 10^{-34}$	
Boltzmann's constant (k) ($J.K^{-1}$)	$1.38 * 10^{-23}$	
Light speed (c) ($m.s^{-1}$)	300000000	

2.2.2. Physicochemical characterization

2.2.2.1. Scanning Electron Microscopy

The morphology of the deposited layers was observed by SEM using a Hitachi model S-4500 SEM with a resolution of 1.5 nm at a voltage of 15 kV. The coupling of the SEM with a Kevex EDS analysis system allowed the quantification of the species present in the deposited coatings, providing a semi-quantitative analysis of the materials.

2.2.2.2. Ion Beam Analysis

For a more in-depth analysis, we used a coupling of Ion Beam Analysis techniques. RBS was used to determine the depth profile of chemical elements in the material, by bombarding the sample placed in a vacuum chamber with an alpha beam $(^4_2He^+)$ of 2 MeV energy. The backscattered alpha particles were detected with a 25 mm² Passivated Implanted Planar Silicon (PIPS) detector located at a 166° angle with respect to the beam axis. The Si and W depth resolution was close to 130.10^{15} at/cm². RBS analyses were completed by NRA and ERDA analyses to get more precise information on the chemical composition of the materials, especially in light elements contents. The oxygen and carbon concentrations were measured by the $^{16}O(d,\alpha_0)^{14}N$ and $^{12}C(d,p_0)^{13}C$ nuclear reactions with 900 keV deuterons at the same detection angle. ERDA was applied with a 2.8 MeV $^4He^+$ beam at 30° angle to determine the hydrogen

depth profile through the nuclear reaction $^{1}H(^{4}He,^{1}H)^{4}He$. The obtained depth resolution for hydrogen oxygen and carbon close to the sample surface was found to be about 300-400.10^{15} at/cm². The depth profiles were extracted from IBA spectra by using SIMNRA software [30] with SigmaCalc cross section [31] for NRA and ERDA. These IBA techniques were carried out using the Pelletron accelerator of CEMHTI laboratory.[32] From these chemical analyses, it was possible to determine the atomic flux of each species present in the material, knowing their atomic concentration. This quantity noted Φ_X corresponds to the atomic flux of the species X incorporated in the material during deposition. It is given by equation 7 where *t* is the deposition time (min), *d* the number of atoms per unit area (at/cm²) and *[X]* the atomic concentration of X, determined by IBA techniques.

$$\Phi_X = \frac{[X] * d}{t} \quad (3)$$

2.2.2.3. X-Ray Photoelectron Spectroscopy

In the same perspective, XPS was used to qualitatively support our chemical analyses. It gave information on the nature and content in chemical elements to obtain a semi-quantitative analysis, and on the nature of the various chemical bonds. The XPS measurements were carried out using a Kratos Axis Nova operating at 1486.6 eV (Al source). After recording wide spectra at a low resolution with pass energy equal to 160 eV to check for any spurious elements, the pass energy and the step scan to measure the region of interest was fixed to 40 eV and 0.1 eV, respectively. The probed depth was 10 nm over a 700×300 µm^2 zone. The dwell times and number of sweeps were chosen such as the highest XPS peak of the selected zone exhibits, at least, 10000 counts. Charge neutralization was used when acquiring the spectra. The energy calibration was set from C 1s signal allotted to carbon linked to W fixed at 283.6 eV since no adventitious carbon (C-C bonds) is detected after etching. Using CasaXPS software [33], after removal of a Tougaard-type background, a Lorentzian Asymmetric lineshape was used for peak fitting. The latter allows numerical convolution of a Lorentzian with a Gaussian to produce a traditional Voigt profile but also an asymmetric Voigt like lineshape. The latter was required to account for the W-C environment expected in the samples. In order to remove the surface pollution, etching using conventional Ar^+ ion gun (2 kV, 70 µA as extracting current) was undertaken according to 3×3 mm^2 raster for 30 s only, in order to avoid beam damages and differential sputtering effect between the elements that could modify chemical information.

3. RESULTS AND DISCUSSIONS

3.1. Process diagnostics

The objective of this study is to identify and monitor by OES the different species present in the gaseous phase. These species are chemical bond carriers in the direction of the growing layer on the substrate holder immersed in the radiofrequency and microwave plasma discharges. This study allows us to understand the growth phenomena resulting in WSiC:H coatings.

3.1.1. Optical emission spectra

Figure 1 superimposes the optical emission spectra measured in: 1) an argon/TMS microwave (MW) plasma in SiC:H PECVD deposition mode, without any source of W; 2) a RF argon plasma during the sputtering of the tungsten target (pure PVD mode); 3) an argon/TMS reactive plasma during the sputtering of the tungsten target, with microwave assistance (reactive MW PVD mode). For this third case, the TMS precursor flow rate was varied from 1% to 20% (0.25 sccm to 5 sccm) of the total gas flow rate (Ar + TMS) maintained constant at 25 sccm, corresponding to a working pressure between 10^{-3} mbar and 10^{-2} mbar. The curves obtained for the different percentages of TMS show the same peaks at the same wavelengths. To lighten the representation, we present only the results for 5 sccm of TMS in Figure 1. This comparison allowed us to identify the main species at play during coating deposition (Table 2). Regarding the SiC:H phase, some of these species result from the direct dissociation of the $Si(CH_3)_4$ precursor, such as CH (431 nm) and H_α (656 nm) which are already present in the precursor, others result from the recombination of these species, such as C_2 (516 nm), H_2 (601 nm) and SiH (415 nm). The emission line at 404 nm is attributed to atomic W, since it is present in both pure PVD mode (W sputtering) and reactive MW PVD mode, but not in SiC:H PECVD deposition mode (Figure 1). Atomic W detected in reactive MW PVD mode is the source for the W incorporation in the growing SiC:H matrix.

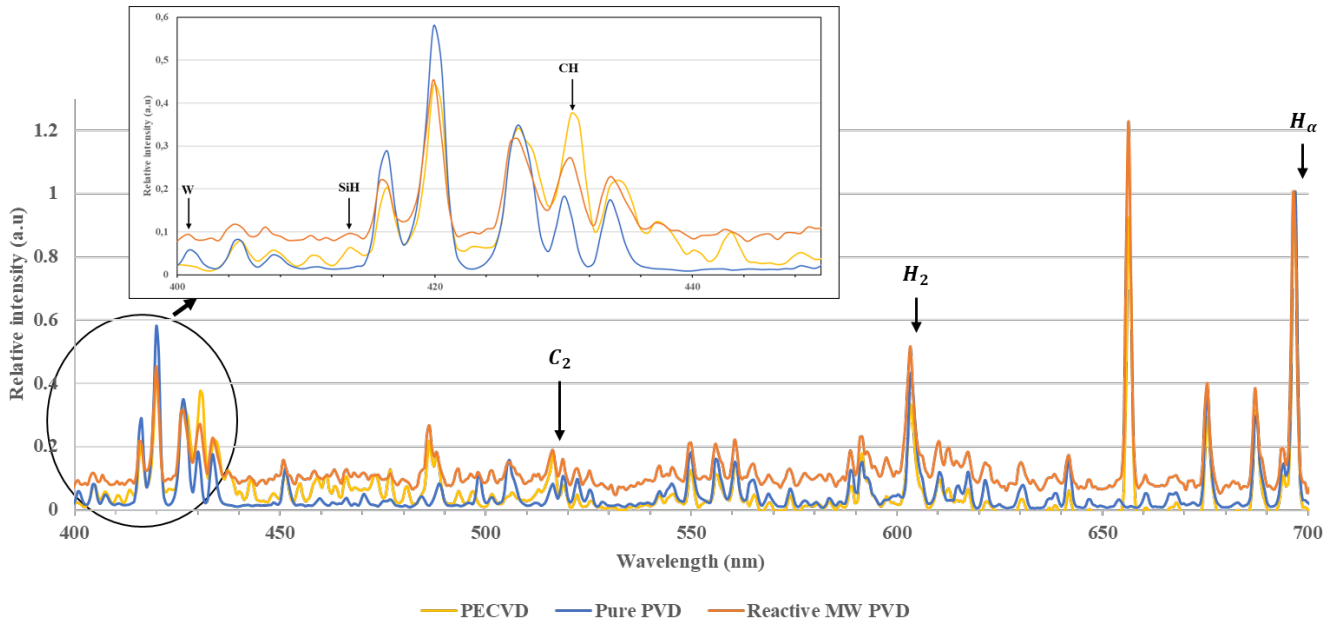

Figure 1: Comparison of Ar + W (pure PVD mode), Ar + TMS (5 sccm, 850 W) (PECVD mode) and Ar + W + TMS (5 sccm, 850 W) (reactive MW PVD mode) plasma emission spectra

Table 2: Identification of emitting species detected by OES in the gaseous phase

Species	*W*	*SiH*	*CH*	C_2	H_2	H_α
Wavelength (nm)	404	415	431	516	601	656

3.1.2. Evolution of electron temperature with precursor flow rate

We have also characterized the reactive MW PVD plasma by studying the electron temperature of the medium. This temperature is related to the emission intensities of species such as argon, through the electron density. It can be useful for a first approach on the behavior of species in the plasma (density evolution, nature of the chemical reactions, etc.).

The values of the electron temperature (Figure 2) in the Ar + W + TMS RF reactive MW PVD plasma are found to be in the range of [0.9 eV; 1.6 eV], which is consistent with the literature for microwave plasmas.[34] For this type of ultra-high frequency plasma, electron densities can be high (up to few 10^{12} electrons/cm^3). This is because electrons, thanks to their low mass, can oscillate at high frequency so as to easily acquire sufficient energy to create ionization cascades that maintain the discharge through collisions. When undergoing these collisions, they lose their energy very quickly, which corresponds to an electron mean temperature of the order of those found in Figure 2. T_e is here an indicator for the dissociation of the TMS precursor. Indeed, this dissociation is ensured by the collisions of energetic electrons from the plasma phase with the precursor molecules. It could be expected that T_e decreases

when injecting a higher quantity of precursor to be dissociated via collisions with the energetic electrons, thus consuming the energy of the latter. Since in our case T_e tends to increase with increasing precursor content (Figure 2), it means that here the dissociation of TMS mainly consumes the low and medium energy electrons of the electron energy distribution function (EEDF), thus leaving mostly the very high energy electrons.[35] As more and more of the lower energy electrons are consumed for precursor dissociation when the TMS flow rate is increased, the mean electron temperature rises due to the higher rate of high energy electrons. Nevertheless, we note that there is a still unexplained and reproducible phenomenon at 8% TMS involving a non-linearity of the T_e curve.

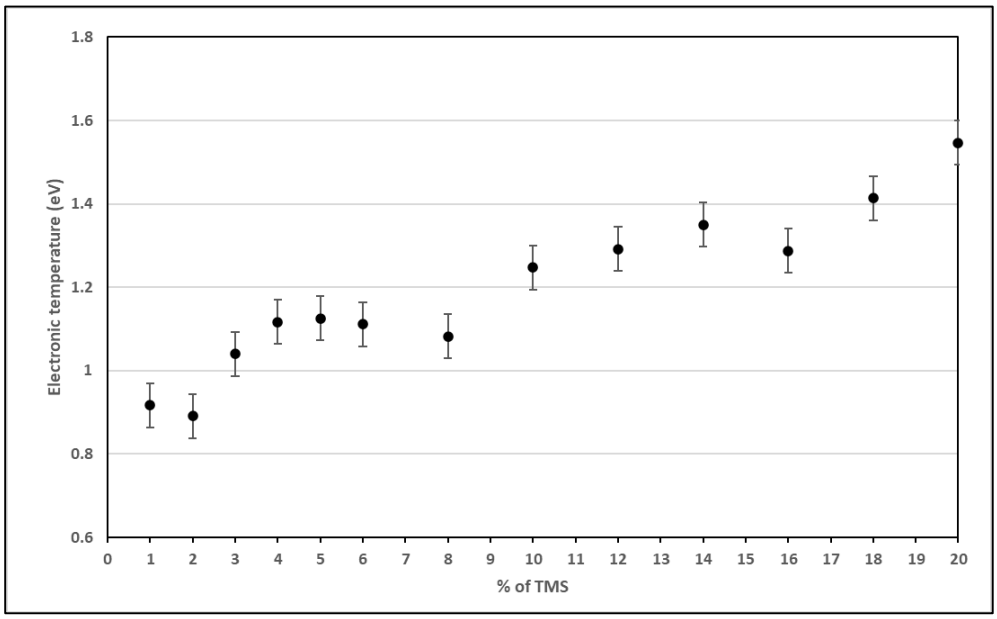

Figure 2: Evolution of the electron temperature of an Ar + W + TMS RF reactive MW PVD plasma with TMS precursor content

3.1.3. Evolution of plasma chemistry with precursor flow rate (actinometry)

We also studied the Ar + W + TMS reactive PVD microwave plasma chemistry as a function of the percentage of TMS injected in the reactor. The emission intensities of each species monitored were normalized according to the principle of actinometry [36], as an indicator of their concentration in the plasma phase. The spectra were acquired during the deposition of the layer, at different times after plasma stabilization (0 min being the first acquisition, then 5 min after the first acquisition and 10 min after the first acquisition).

3.1.3.1. Species resulting from precursor dissociation

For the species directly resulting from the dissociation of TMS ($Si(CH_3)_4$), H_α among others which are optical tracers representative of the dissociation of the precursor (Figure 3), there is an increase in concentration with the increase of TMS content. This is expected in that the more TMS is injected into the reactor, the more it dissociates. This also means that the electrons from the discharge are able to dissociate efficiently the TMS molecules whatever the percentage injected in the reactor in the range [1%-20%]. Furthermore, we observe that overall, at a fixed percentage of TMS, whatever the duration of the deposition, the plasma chemistry remains unchanged regarding the dissociation of the TMS precursor. This stability with time is very useful, since it allows us to have a margin of error on the deposition duration and to adapt the deposited layer thicknesses depending on the application.

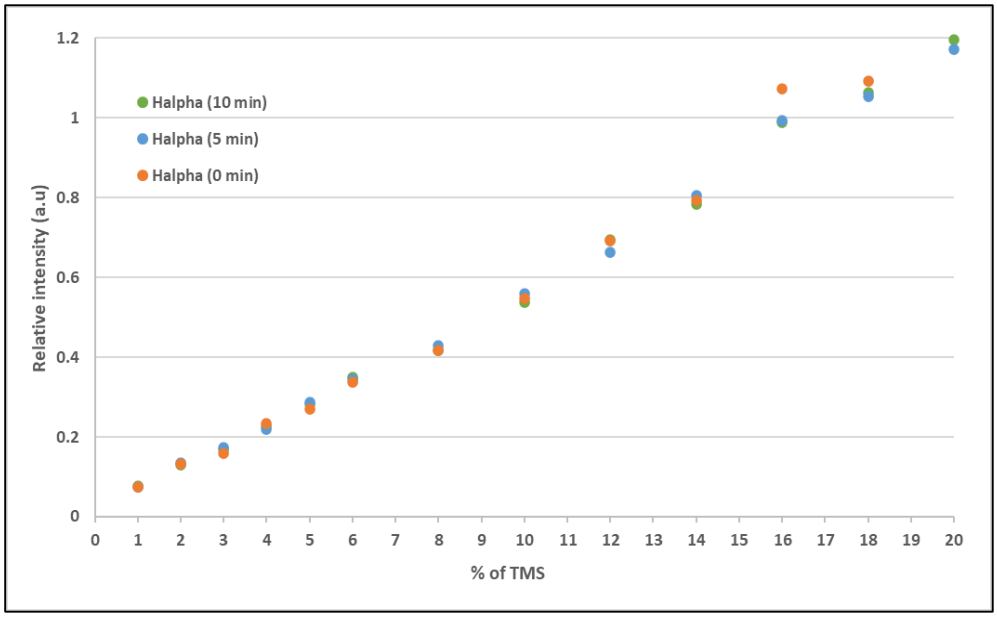

Figure 3: Evolution of the concentration of H_α species representing the dissociation of TMS precursor ($Si(CH_3)_4$) in the Ar + W + TMS reactive PVD microwave plasma, vs. TMS content, for different deposition durations

3.1.3.2. Species resulting from target sputtering

Introducing TMS precursor during W sputtering induces a possible pollution of the target, which can lead to a modification of the target surface, as the reaction of the gas with the surface leads to the formation of a compound made of metal and species from the gaseous precursor, which is then sputtered instead of the pure metal. This change in the target surface state, induced by the presence of the reactive gas, leads to a change in the physical properties of the target such as the sputtering rate or the secondary electronic emission.

To study if this phenomenon occurs in our case, we followed the evolution of atomic W emission, i.e., the species resulting from the sputtering of the W target, with the percentage of TMS precursor injected in the gas phase. Figure 4 shows the evolutions of W relative intensity versus time and %TMS in the discharge mixture. The W emission globally tends to increase with the increase in the percentage of TMS. This can mean that the percentage of TMS is low enough so that the process remains in a pure target sputtering regime whatever the TMS flow rate, and not a compound sputtering regime (in other words, the target is not polluted by the deposition of a metal/ceramic compound from the reactive plasma phase). This phenomenon can be explained by the increase in W emission intensity with %TMS which could also be related to the increase in the electron temperature with increasing TMS flow rate (Figure 2), as high-energy electrons are available for the excitation of W while low-energy electrons are consumed for precursor dissociation.

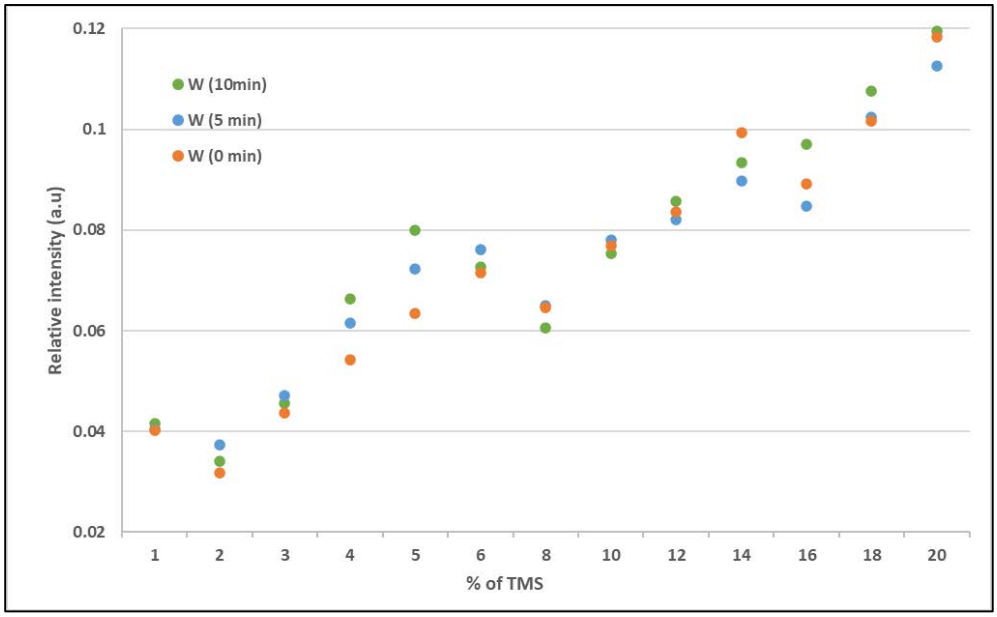

Figure 4: W intensity as a function of TMS percentage at different times in Ar + W + TMS plasma

W relative intensity does not vary linearly with %TMS (Figure 4). Two remarks can be made: 1) W relative intensity unexpectedly decreases at intermediate %TMS values; 2) contrarily to what was observed regarding plasma chemistry (species representative of precursor dissociation in Figure 3), W relative intensity is time dependent. Meanwhile, powders have been collected in the reactor after measurements (Figure 5). SEM/EDS analyses conclude that these powders are constituted of aggregates of nanoparticles with 42% of W, 56% of C, 1% of O and 1% of Si. This formation of W containing particles in the discharge is consistent with OES measurements, as the growth of W powders in the

plasma phase during deposition can lead to the observed decrease of emitting W atoms in time at intermediate %TMS (Figure 4), the latter being “consumed” to form powders in the discharge, that cannot be detected by OES.

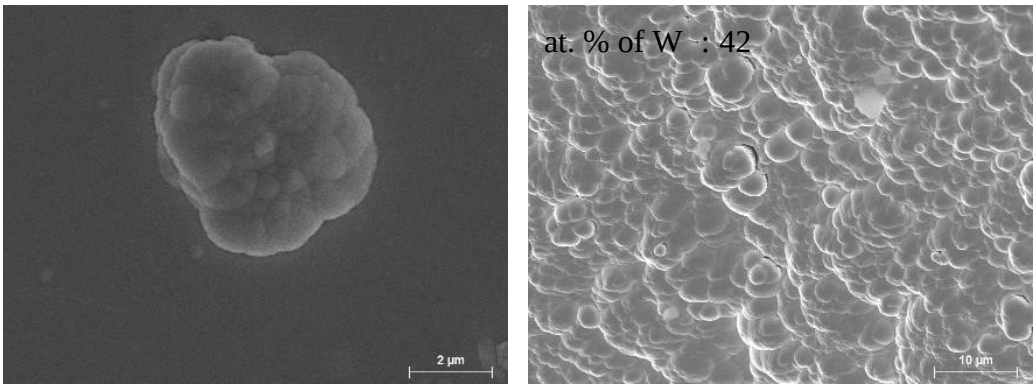

Figure 5: SEM images of powders collected in the reactor after reactive PVD deposition with 5 sccm of TMS and 850 W of microwave power

3.1.4. Conclusions on process diagnostics

All in all, it appears that for this reactive PVD deposition process, there is a domain of precursor flow rate (%TMS) where W particles can be favored inside the reactive plasma process, to promote the elaboration of composite coatings based on a SiC:H matrix containing metallic W particles or aggregates. Such information is useful to determine the potential of the process to deposit a WSiC:H compound in a specific experimental domain. Thanks to the previous observations, we can deduce that in the medium range of %TMS (from 6% to 18% of TMS precursor in the injected gas mixture with total flow rate of 25 sccm) it is possible with this process to obtain W particles in the gas phase, as the target surface is not completely saturated so that a pure sputtering mode is maintained. Such a process could then be used to obtain cermet-like materials, by incorporating these W particles in the SiC:H matrix.

In view of these results, the impact of the changes in the gas phase on the physicochemical properties of the deposited materials is also studied, to correlate the phenomena in the gas phase and the growth mechanisms of the coatings, as well as the corresponding microstructure of the materials.

3.2. WSiC:H coatings characterization

Series of W/WSiC:H coatings were deposited and characterized. Depending on the sample, the TMS precursor flow rate in the Ar/TMS gas mixture during WSiC:H deposition ranges from 0.25 sccm to 5 sccm (from 1% to 20% of the total gas flow rate of 25 sccm in the reactor) and the deposition duration is adapted to have 180 nm of thickness for each WSiC:H layer.

3.2.1. Morphology (SEM)

As an illustration, Figure 6 presents the cross-section SEM images for samples synthesized with 1%, 8% and 20% of TMS (i.e., 0.25 sccm, 2 sccm and 5 sccm of TMS in the plasma Ar/TMS mixture).

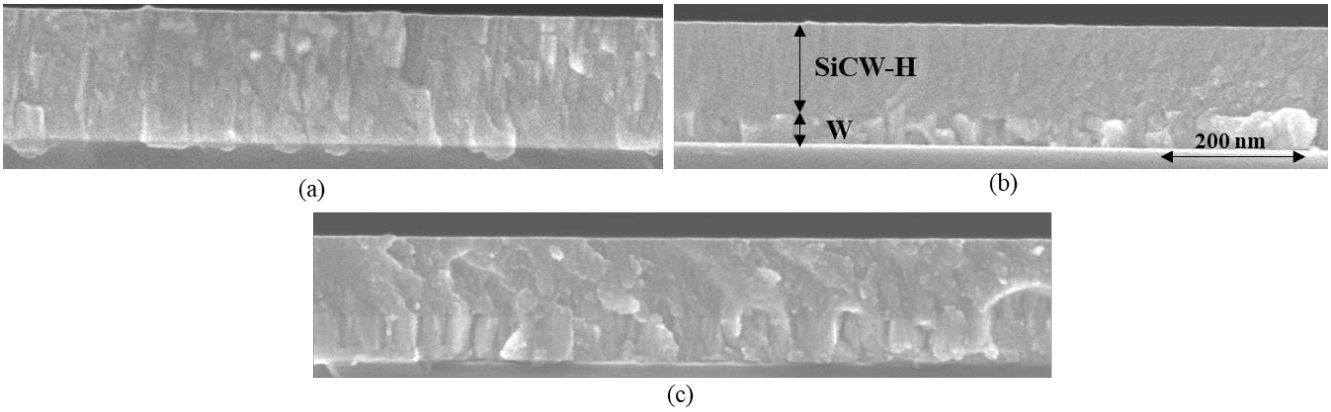

Figure 6: Cross-section SEM images of samples deposited with (a) 1%, (b) 8% and (c) 20% of TMS in the Ar/TMS plasma for the WSiC:H top layer

In Figure 6, the samples present two layers that grow differently due to the different deposition processes (RF PVD for the W sublayer and reactive PVD with microwave source assistance for the top layer), with a columnar growth for the W underlayer. At lower TMS flow rates (from 1% to 4%, represented by Figure 6 (a)), the interface between the two layers is not very clear and the whole coating seems homogeneous. Between 5% and 18% of TMS, the interface between layers is much clearer, with the WSiCH layer having a granular appearance while the W sublayer is columnar (as seen in Figure 6 (b) for 8% TMS). At 20%, the layers are again not clearly separated (Figure 6 (c)).

3.2.2. Chemical composition (EDS, IBA, XPS)

EDS measurements (Figure 7) give information on the overall chemical composition of the samples. The layers are mostly formed of carbon, whose atomic content rises between 50 at.% and 60 at.%, much more

than silicon content. This can be explained by the fact that there is more four times carbon than silicon in the gas precursor. The absolute Si and W atomic contents cannot be considered here due to the Si nature of the substrate and the presence of the W sublayer. The latter are indeed detected within the interaction bulb of the SEM used for these analyses (# 1 µm in depth, much larger than the coating thickness). Nevertheless, since the thickness are identical we can consider that the incorporation of Si in the coatings starts at least from 10% of TMS in the plasma, coinciding with the decrease of the detected W content (Figure 4). This hypothesis can be supported by the observations made in OES where the drastic increase of T_e from 10% refers to a consumption of low energy electrons and thus to a more important dissociation of the TMS.

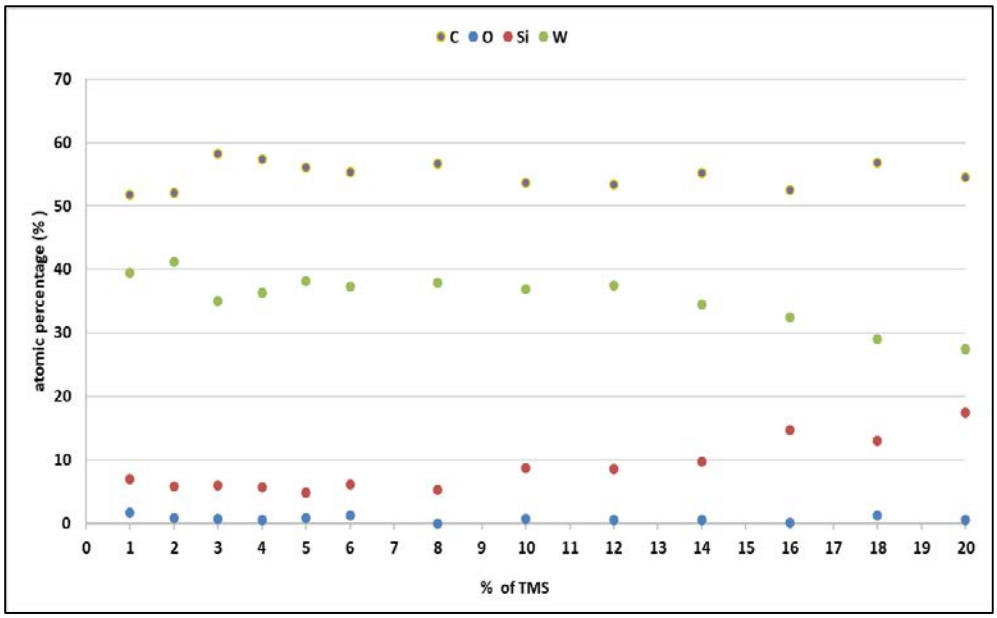

Figure 7: Chemical composition of the deposited coatings determined by EDS analysis as a function of the percentage of TMS injected in the reactor during reactive MW PVD deposition

To go deeper in the coatings analysis, we referred to NRA, ERDA and RBS methods to find out their in-depth chemical composition. These analyses allowed us to take a different look at the materials. For the analysis of the results, all the samples were considered to be constituted of four layers, L1 to L4, as shown in Figure 8. Even if the substrate was cleaned by Ar plasma before deposition, we notice a SiO_2 noted L1 underlayer which corresponds to the natural oxidation of the Si substrate surface before W layer deposition. It is systematically present on all samples with a number of atoms per unit area close to 20.10^{15} at/cm². The composition profiles of the two stacked thin films (supposedly W and WSiC:H) are represented by three layers (L2 to L4). The L3 layer is the main SiCW material, L2 is the first layer

deposited on the substrate (supposedly W) and L4 the layer that we supposed to be a part of L3 which is oxidized by the exposition to air.

Figure 8: Sample layout considered for the interpretation of IBA simulations

3.2.2.1. Composition of the L2 "W:C" layer (Figure 9)

We find for this layer an average number of atoms per unit area of 593 ±13 x $10.^{15}$ at/cm² with 95.8 ± 1.5 at.% W. This sublayer is intended to be composed of 100% W as it corresponds to the pure PVD mode (sputtering of W target in Ar plasma). However, we detected a low amount of carbon (5.2 ± 1.5 at.%) in this layer in all samples. This carbon could either come from residues present in the reactor before the deposition (even if it is cleaned before each deposition) or from the SiCW layer deposited above, due to atomic diffusion during the synthesis at 350°C. A study of the chemical composition of the W layer as a separate layer would be appropriate to obtain more information about the carbon present in this layer.

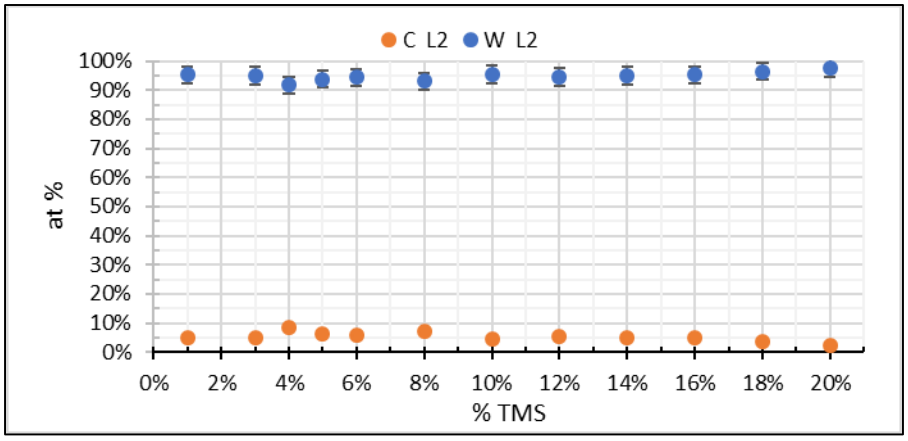

Figure 9: Chemical composition of "W:C" L2 layer measured by IBA

3.2.2.2. Composition of the L4 "SiCWOH" top layer

3.2.2.2.1. IBA analyses (Figure 10)

For all samples, we detected and measured hydrogen and oxygen onto the surface, with a number of atoms per unit area of 230 to 290 x 10^{15} at/cm². The concentration of hydrogen varies between 6 and 8 at.% and that of oxygen between 3 and 7 at.%. This estimated atomic amount is of the order of magnitude of the depth resolution of the NRA and ERDA techniques. It is likely that this hydroxide layer is actually thinner, with higher O and H concentrations as observed by XPS analysis (see below). Its formation is believed to be due to a slight adsorption of water and/or hydroxyl after deposition.

As suspected from EDS measurements (Figure 7), the presence of silicon is only observed starting from a significant amount of precursor in the discharge, here 8% TMS. Si content in this layer then increases as expected with the increase of TMS flow rate. For the main elements in L4, C and W, a plateau is observed between 3 and 14% TMS, with average values of 51.9 ± 2.2 at.% for W and 33.9 ± 2.9 at.% for carbon. Above 14% TMS, we notice an increase of C due to the increase of the TMS injected in the reactor and a decrease of W, with nevertheless a convergence in the atomic content of these two elements at 20% of TMS.

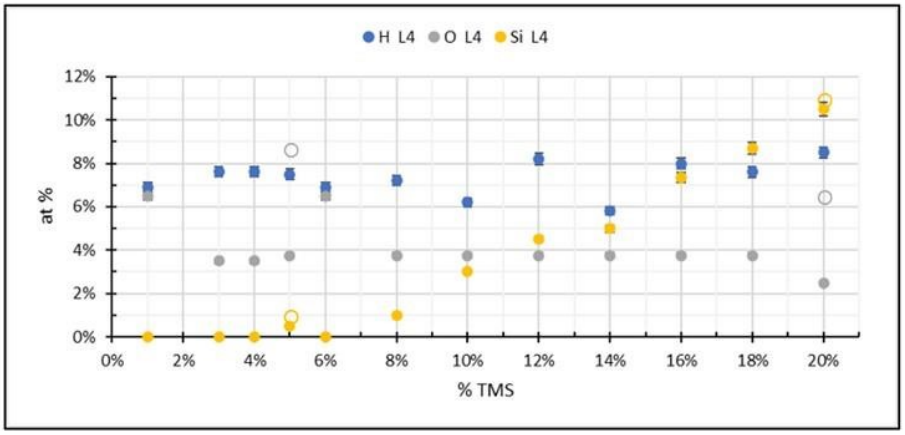

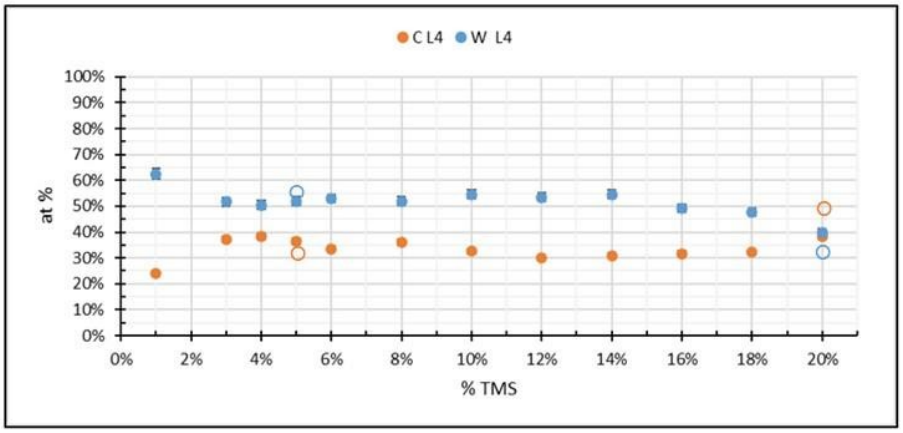

Figure 10: Chemical composition of L4 “SiCWOH” layer measured by IBA (closed circle) and by XPS (open circle)

3.2.2.2.2. XPS analyses

To confirm the amount of oxygen in L4 layer detected by RBS, XPS analyses were performed in order to get information about the chemical bonds present at the surface of coatings elaborated with 5% and 20% of TMS, respectively, thus investigating a TMS percentage in each of the abovementioned groups. The measurements were carried out on the pristine sample to get information on L4 layer (as defined in Figure 8) and after etching for 30 seconds to minimize the surface contamination due to storage conditions. The results presented in Figure 11 show the spectra obtained for the levels O 1s, C 1s, Si 2p and W 4f whose decomposition gives us the different environments contained in the materials and their stoichiometry.

For the 5%TMS sample, O 1s can be decomposed into O,OH-Si (from SiO_x) at 532.4 eV and O,OH-W (from WO_x species) at 531.3 eV. The binding energies of 285.1 eV and 283.6 eV can respectively be assigned to C-C/C-H and C-W bonds [37]. Environments typical of C-O and C=O are also identified at 287.0 eV and the peak at 289.6 eV may arise from the formation of carbonate complex due to interaction with atmospheric CO_2. Si-O bond is characterized by its 2p1/2 and 2p3/2 peaks located at 103.2 eV and 102.6 eV, respectively, on the surface of this sample. The decomposition of W 4f7/2 peak shows W-O bond at 36.5 eV and W linked to C at 32.2 eV (W 4f5/2 at 38.6 and 34.3 eV, respectively). After etching, in agreement with [37] and [38], we mostly find W-C bonds at 31.8 and 34.0 eV (for W 4f7/2 and 4f5/2 respectively) after removal of the surface contamination and a very low amount of Si compared to previous analysis. This is consistent with the results obtained in RBS for this category of %TMS, with a high W content (Figure 10). For the sample elaborated with 20% of TMS, we find at the surface the same elements as for the 5%TMS, with in addition Si bound to C at 101.1 eV after the decomposition of Si 2p signal. The attribution of the C1s component detected at 284.4 eV after etching needs complementary study. However, since TMS encompasses 4 methyl group per Si atom we cannot exclude the deposition of carbon-rich zones whose nature needs to be clarified. After removal of the surface contamination, we again have W-C environment, accompanied by Si bound to C and O. This confirms the incorporation of silicon in this coating elaborated with 20% of TMS and is also coherent with IBA results (Figure 10).

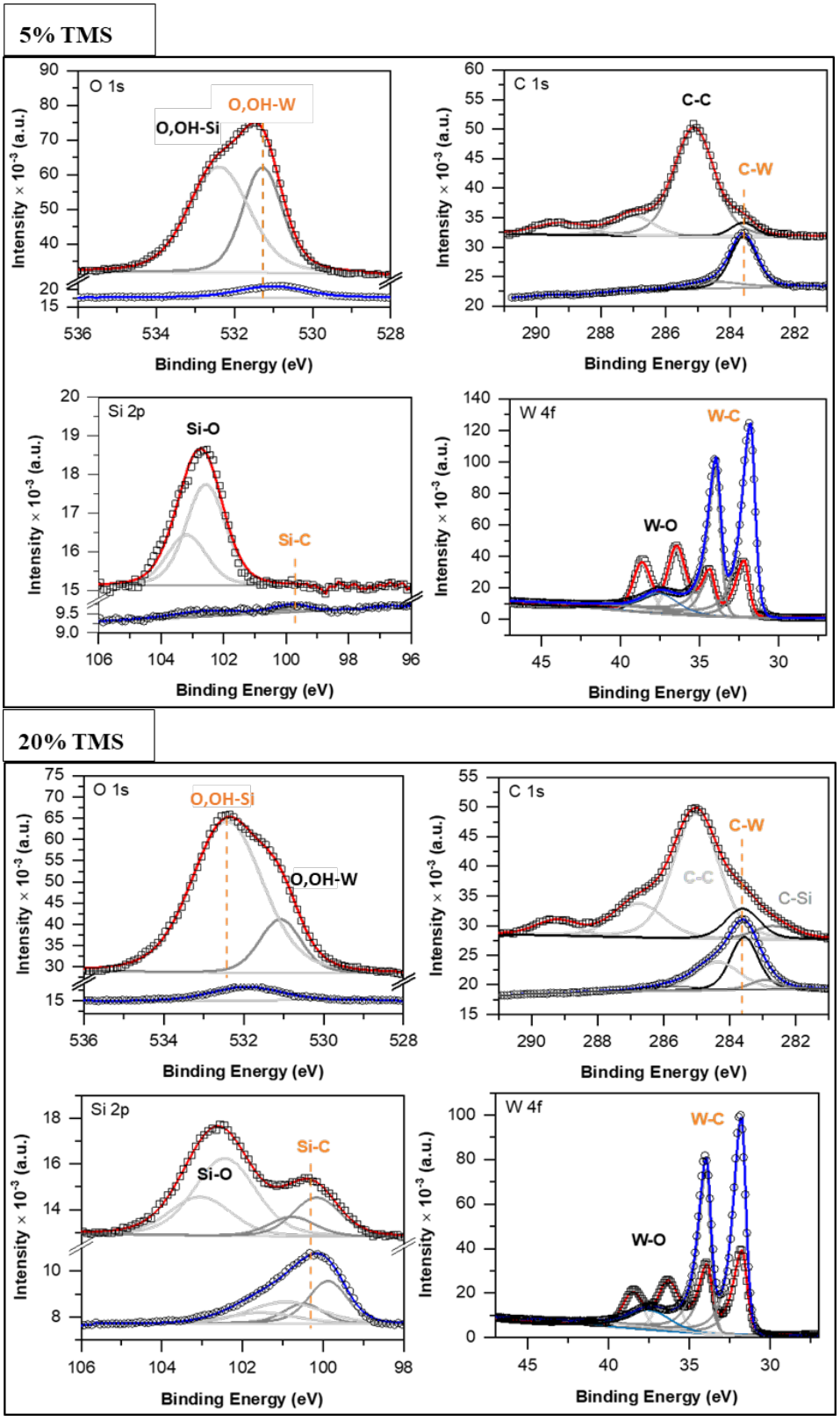

Figure 11: Experimental XPS spectra of the topmost L4 layer (squares) and after erosion for 30 s (circles) of samples elaborated with 5 % and 20% of TMS and fitted components (grey lines) with the total fitted envelop before (red line) and after etching (blue line).

The analysis of the main components in the samples before and after etching showed the surface stoichiometries (chemical formulae) gathered in Table 3. The W 4f peaks attributed to carbide bonds (at 31.8 and 34.0 eV) were used as reference for the W-C contribution, as they are detected in all cases. The numbers before brackets are molar ratios, obtained by dividing the atomic percentage of each element by the sum of the two atomic percentages of W and C in W-C bonds in the W 4f peak.

Table 3: Composition of samples elaborated with 5% and 20% of TMS according to XPS characterization. The W 4f peaks attributed to W-C bonds were used as reference.

Sample	*Before etching (surface of L4 layer)*	*After etching for 30 sec (L4 layer)*
5 %	$1.34[W\text{-}O_x]/[W\text{-}C_{0.5}]/0.9[Si\text{-}O_x]$	$[W\text{-}C_{0.5}]$
20 %	$0.74[W\text{-}O_x]/[W\text{-}C_{0.9}]/0.5[Si\text{-}C_{1.6}]/1.34[Si\text{-}O_x]$	$[W\text{-}C_x]/0.19[Si\text{-}C_{0.5}]/0.19[Si\text{-}O_y]$

To conclude on this part, at high percentage of TMS precursor, W and Si are each bound to C. This means that Si in the films certainly comes from the direct plasma dissociation of TMS and not from the sputtering of a target poisoned with a WSiCH compound, or otherwise we would detect Si-W bonds as well. However, the W target seems to be poisoned by carbon-containing species which are logically more numerous in the gas phase due to the fact that there is four times more carbon than silicon in the precursor ($Si(CH_3)_4$), creating a WC film on its surface which is sputtered towards the substrate. This explains the WC bonds observed in XPS for this layer.

3.2.2.3. Composition of the L3 "SiCW" layer (Figure 12)

The main layer contains only the elements Si, C and W with a majority for the last two and its number of atoms per unit area is in between 1120 to 1890 x 10^{15} at/cm². Again, the presence of Si is only observed above 8% TMS, then the Si content increases with increasing TMS flow rate, up to a maximum of 10 at.% for 20% TMS in the plasma phase. For W, a plateau is observed between 3 and 14% TMS with an average concentration of 58.3 ± 0.7 at.%. The value of carbon concentration remains relatively the same at 40.0 ± 2.3 at.% for the whole series. Above 14% TMS, the W content then naturally decreases as Si content tends to increase.

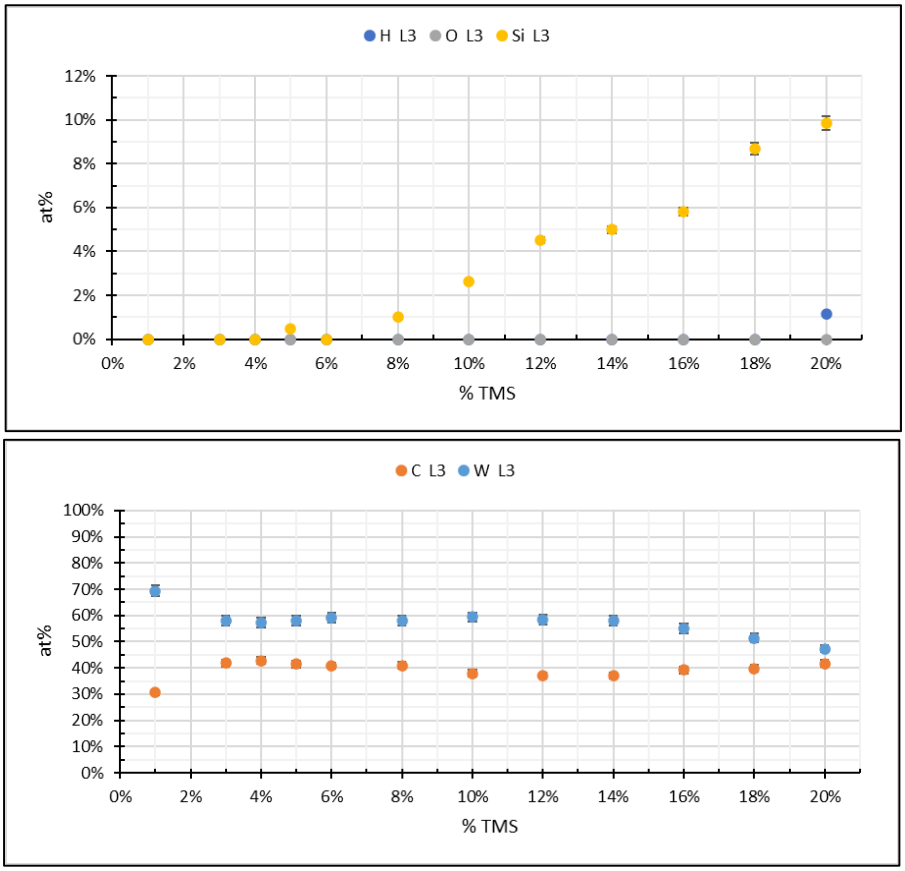

Figure 12: Chemical composition of L3 “SiCW” layer measured by IBA

To go further and understand these microstructures of these materials, we have plotted the estimated atomic flux (Figure 13) of W and Si, i.e., the number of atoms of these species incorporated in the materials as a function of the deposition duration. This quantity is the product between the atomic percentages of these elements, the layer atomic amount (at/cm²) and the deposition duration (min) for the L3 SiCW layer and L4 top layer.

At a very low percentage of TMS, i.e., between 1% and 8%, the content of W is rather constant. This confirms the previous hypothesis that in this flow range the W target is not polluted by a metal/ceramic compound deriving from TMS dissociation. From 10% TMS onwards, the flux of W decreases markedly and that of silicon increases. This drop of W incorporation, while the sputtering power is constant, could indicate the target poisoning in this range.

Considering the content of W and Si in the top layers of the coatings, we can identify two groups of TMS percentages: the group with a percentage below 10%TMS for which mostly W is incorporated in the film, and the group above 10%TMS for which we start to incorporate Si.

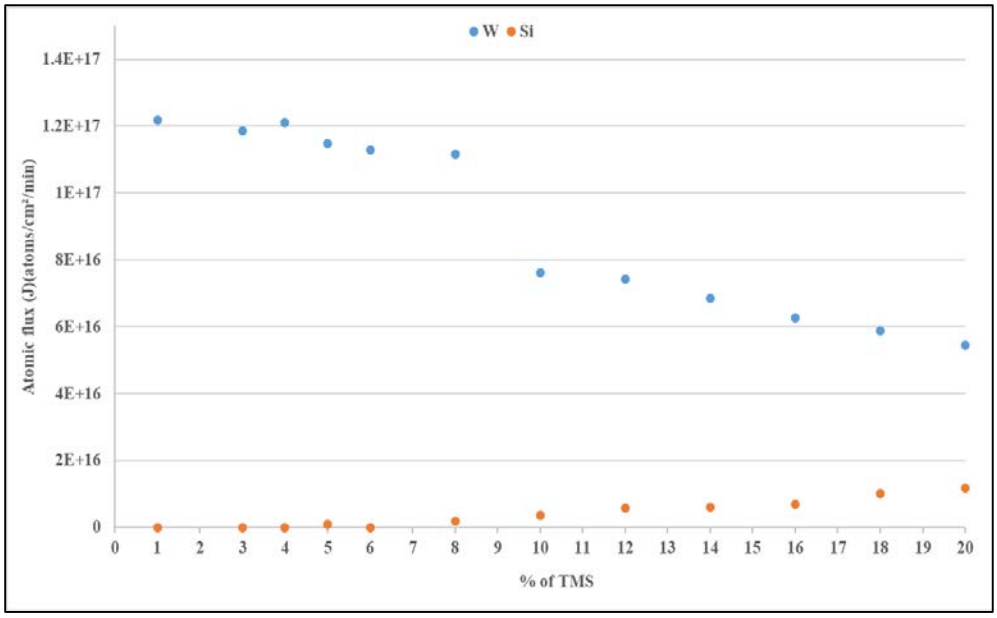

Figure 13: Atomic flux of W and Si as a function of the percentage of TMS precursor during reactive PVD MW deposition, estimated from IBA measurements

4. Conclusions

WSiCH coatings were elaborated by the reactive RF sputtering of a W target in an Ar/Si$(CH_3)_4$ plasma assisted by ECR microwave sources. The points discussed in this first paper show the complexity of these materials, both in terms of the plasma chemistry leading to its elaboration and its resulting chemical composition due to the simultaneous sputtering of the target and dissociation of the reactive gas, but allowed us to estimate the conditions for which the development of these cermets is feasible.

Process diagnostics performed by optical emission spectroscopy showed the ability to form powders in the gas phase. Investigations showed a poisoning of the W target by C forming W-C aggregates towards the growing layer. These results are supported by the chemical analyses performed on the samples from this gas phase. Indeed, the IBA analyses showed very high amounts of W and C compared to that of Silicon. The XPS measurements carried out on the top layer (SiCWOH) also highlighted this formation of W-C bonds.

The correlation between the process diagnostics and the material characterizations allowed us to estimate the conditions in terms of percentage of TMS for which the development of tungsten-containing nanoparticles incorporated in a SiC matrix is feasible, insofar as silicon is effectively detected from 10% TMS. In future work, the formation of such nanocomposites will be investigated by TEM.

Such cermets could be considered for spectrally selective absorber materials used to improve the thermo-optical performance of concentrating solar power plant receivers.[11,39–41] Indeed, the inclusion of

metallic nanoparticles can lead to the appearance of evanescent waves resulting from the plasmonic effect [7,42–44] within the material when it is illuminated, increasing its absorbing power. In the continuity of this work, we will in fact consider in our next paper their insertion in a multilayer coating architecture with a top antireflective layer of TaO_xN_y,[45,46] for which first optical simulations and optical measurements proved promising performance for the receivers of concentrated solar power plants.

Acknowledgments

This work was financed by the French National Research Agency (ANR), as part of the NANOPLAST project (nanoplast-project.cnrs.fr) under contract ANR-19-CE08-0019, and the "Investments for the future" programme under contract ANR-10-LABX-22-01-SOLSTICE. The authors thank C. Escape, Y. Gorand, E. Hernandez, H. Glénat, O. Wendling, A. Bellamy and all the technical partners for their involvement.

References

[1] A.J. Gant, M.G. Gee, A.T. May, The evaluation of tribo-corrosion synergy for WC–Co hardmetals in low stress abrasion, Wear. 256 (2004) 500–516. https://doi.org/10.1016/j.wear.2003.04.001.

[2] N.K. Singh, A.S.M. Ang, D.K. Mahajan, H. Singh, Cavitation erosion resistant nickelbased cermet coatings for monel K-500, Tribology International. 159 (2021) 106954. https://doi.org/10.1016/j.triboint.2021.106954.

[3] A.Q. Li, N. Lin, L.W. Xu, W.J. Zhang, X.C. Zhang, Z.Y. Wang, C. Ma, Improvement mechanism of the oxidation resistance of Al-doped Ti(C,N)-based cermets: Influence of enriched Al in the subsurface oxide layer, Corrosion Science. 209 (2022) 110722. https://doi.org/10.1016/j.corsci.2022.110722.

[4] L. Jie, Gang ZHANG, Shao-long YE, Yan-qin LAI, Zhong-liang TIAN, Xiao-gang SUN, Effect of metallic content on mechanical property of Ni/(10NiO-NiFe204) cermets®, 13 (2006) 6.

[5] G. Zhang, J. Li, Y. Lai, Z. Tian, Effect of metallic phase content on mechanical properties of (85Cu-15Ni)/(10NiO-NiFe2O4) cermet inert anode for aluminum electrolysis, Transactions of Nonferrous Metals Society of China. 17 (2007) 1063–1068. https://doi.org/10.1016/S1003-6326(07)60226-X.

[6] T.S. Sathiaraj, R. Thangaraj, H.A. Sharbaty, M. Bhatnagar, Ni-AI20 3 SELECTIVE CERMET COATINGS FOR PHOTOTHERMAL CONVERSION UP TO 500 °C, (n.d.)
14.
[7] H.C. Barshilia, P. Kumar, K.S. Rajam, A. Biswas, Structure and optical properties of Ag– Al2O3 nanocermet solar selective coatings prepared using unbalanced magnetron sputtering, Solar Energy Materials and Solar Cells. 95 (2011) 1707–1715. https://doi.org/10.1016/j.solmat.2011.01.034.
[8] G.A. Nyberg, H.G. Craighead, R.A. Buhrman, Surface roughness and thermal stability of graded cermet photothermal absorber coatings with very high absorptivities, Thin Solid Films. 96 (1982) 185–190. https://doi.org/10.1016/0040-6090(82)90619-8.
[9] G.A. Niklasson, C.G. Granqvist, Optical properties and solar selectivity of coevaporated Co- Al 2 O 3 composite films, Journal of Applied Physics. 55 (1984) 3382–3410. https://doi.org/10.1063/1.333386.
[10] J. Lafait, S. Berthier, C. Sella, T. Vien, Pt Al2O3 selective absorber coatings for photothermal conversion up to 600°C, Vacuum. 36 (1986) 125–127. https://doi.org/10.1016/0042-207X(86)90285-X.
[11] A. Antonaia, A. Castaldo, M.L. Addonizio, S. Esposito, Stability of W-Al2O3 cermet based solar coating for receiver tube operating at high temperature, Solar Energy Materials and Solar Cells. 94 (2010) 1604–1611. https://doi.org/10.1016/j.solmat.2010.04.080.
[12] D. Ngoue, A. Grosjean, L. Di Giacomo, S. Quoizola, A. Soum-Glaude, L. Thomas, Y. Lalau, R. Reoyo-Prats, B. Claudet, O. Faugeroux, C. Leray, A. Toutant, J.-Y. Peroy, A. Ferrière, G. Olalde, Ceramics for concentrated solar power (CSP): From thermophysical properties to solar absorbers, in: Advanced Ceramics for Energy Conversion and Storage, Elsevier, 2020: pp. 89–127. https://doi.org/10.1016/B978-0-08-102726-4.00003-X.
[13] L. Rebouta, A. Sousa, P. Capela, M. Andritschky, P. Santilli, A. Matilainen, K. Pischow, N.P. Barradas, E. Alves, Solar selective absorbers based on Al2O3:W cermets and AlSiN/AlSiON layers, Solar Energy Materials and Solar Cells. 137 (2015) 93–100. https://doi.org/10.1016/j.solmat.2015.01.029.
[14] E. Wuchina, E. Opila, M. Opeka, B. Fahrenholtz, I. Talmy, UHTCs: Ultra-High Temperature Ceramic Materials for Extreme Environment Applications, Electrochem. Soc. Interface. 16 (2007) 30–36. https://doi.org/10.1149/2.F04074IF.
[15] Pro-men, The degree of oxidation of tungsten. Tungsten in nature., Promen. (n.d.).

https://pro-men.ru/fr/the-degree-of-oxidation-of-tungsten-tungsten-in-nature/ (accessed March 10, 2022).

[16] Britannica, tungsten | Uses, Properties, & Facts, (n.d.). https://www.britannica.com/science/tungsten-chemical-element (accessed March 28, 2022).

[17] M. Henini, Handbook of Thin-Film Deposition Processes and Techniques, Microelectronics Journal. 31 (2000) 219. https://doi.org/10.1016/S0026-2692(99)00122-6.

[18] A. Chesnaud, F. Karolak, C. Bogicevic, S. Phothirath, C. Estournès, G. Dezanneau, Densification par Spark Plasma Sintering (SPS) de matériaux d'électrolytes, difficilement densifiables, pour piles à combustible, Mater. Tech. 95 (2007) 259–268. https://doi.org/10.1051/mattech:2008010.

[19] E. Braval, C.G. Pantano, Sol-gel prepared Ni-alumina composite materials, Journal of Materials Science. 27 (1992) 7.

[20] J. Gonzlez-Gutirrez, G. Beulke, I. Emri, Powder Injection Molding of Metal and Ceramic Parts, in: J. Wang (Ed.), Some Critical Issues for Injection Molding, InTech, 2012. https://doi.org/10.5772/38070.

[21] J. Jyothi, H. Chaliyawala, G. Srinivas, H.S. Nagaraja, H.C. Barshilia, Design and fabrication of spectrally selective TiAlC/TiAlCN/TiAlSiCN/TiAlSiCO/TiAlSiO tandem absorber for high-temperature solar thermal power applications, Solar Energy Materials and Solar Cells. 140 (2015) 209–216. https://doi.org/10.1016/j.solmat.2015.04.018.

[22] M. Du, X. Liu, L. Hao, X. Wang, J. Mi, L. Jiang, Q. Yu, Microstructure and thermal stability of Al/Ti0.5Al0.5N/Ti0.25Al0.75N/AlN solar selective coating, Solar Energy Materials and Solar Cells. 111 (2013) 49–56. https://doi.org/10.1016/j.solmat.2012.12.010.

[23] C. Doland, P. O'Neill, A. Ignatiev, Particulate nature of solar absorbing films: Gold black, Journal of Vacuum Science and Technology. 14 (1977) 259–262. https://doi.org/10.1116/1.569135.

[24] J.P. Celis, D. Drees, M.Z. Huq, P.Q. Wu, M. De Bonte, Hybrid processes — a versatile technique to match process requirements and coating needs, Surface and Coatings Technology. 113 (1999) 165–181. https://doi.org/10.1016/S0257-8972(98)00836-6.

[25] A. Soum-Glaude, L. Thomas, S. Quoizola, L. Di Giacomo, E. Hernandez, Reactor for depositing layers and associated deposition process, WO2019097023A1, 2019.

[26] Avantes, AvaSpec-ULS2048XL-EVO, (n.d.).

https://www.avantes.com/products/spectrometers/sensline/avaspec-uls2048xl-evo/ (accessed March 3, 2022).

[27] Avantes, AvaSoft-Basic, (n.d.). https://www.avantes.com/products/software/avasoft-basic/ (accessed March 3, 2022).

[28] G. Zambrano, H. Riascos, P. Prieto, E. Restrepo, A. Devia, C. Rincón, Optical emission spectroscopy study of r.f. magnetron sputtering discharge used for multilayers thin film deposition, Surface and Coatings Technology. 172 (2003) 144–149. https://doi.org/10.1016/S0257-8972(03)00339-6.

[29] 3.1.2: Maxwell-Boltzmann Distributions, Chemistry LibreTexts. (2013). https://chem.libretexts.org/Bookshelves/Physical_and_Theoretical_Chemistry_Textbook_Maps/Supplemental_Modules_(Physical_and_Theoretical_Chemistry)/Kinetics/03%3A_Rate_Laws/3.01%3A_Gas_Phase_Kinetics/3.1.02%3A_Maxwell-Boltzmann_Distributions (accessed March 28, 2022).

[30] M. Mayer, SIMNRA, a simulation program for the analysis of NRA, RBS and ERDA, in: AIP Conference Proceedings, AIP, Denton, Texas (USA), 1999: pp. 541–544. https://doi.org/10.1063/1.59188.

[31] A.F. Gurbich, SigmaCalc recent development and present status of the evaluated crosssections for IBA, Nuclear Instruments and Methods in Physics Research Section B: Beam Interactions with Materials and Atoms. 371 (2016) 27–32. https://doi.org/10.1016/j.nimb.2015.09.035.

[32] Pelletron et Cyclotron - EMIRA, (n.d.). https://emira.ijclab.in2p3.fr/pelletron-et-cyclotron/ (accessed July 20, 2022).

[33] N. Fairley, V. Fernandez, M. Richard‐Plouet, C. Guillot-Deudon, J. Walton, E. Smith, D. Flahaut, M. Greiner, M. Biesinger, S. Tougaard, D. Morgan, J. Baltrusaitis, Systematic and collaborative approach to problem solving using X-ray photoelectron spectroscopy, Applied Surface Science Advances. 5 (2021) 100112. https://doi.org/10.1016/j.apsadv.2021.100112.

[34] L. Latrasse, Conception, caractérisation et applications des plasmas micro-onde en configuration matricielle, Université Joseph Fourier, 2006.

[35] Z. Chen, V.M. Donnelly, D.J. Economou, L. Chen, M. Funk, R. Sundararajan, Measurement of electron temperatures and electron energy distribution functions in dual frequency capacitively coupled CF4/O2 plasmas using trace rare gases optical emission spectroscopy, Journal of

Vacuum Science & Technology A: Vacuum, Surfaces, and Films. 27 (2009) 1159–1165. https://doi.org/10.1116/1.3179162.

[36] J.W. Coburn, M. Chen, Optical emission spectroscopy of reactive plasmas: A method for correlating emission intensities to reactive particle density, Journal of Applied Physics. 51 (1980) 3134–3136. https://doi.org/10.1063/1.328060.

[37] G. Greczynski, D. Primetzhofer, L. Hultman, Reference binding energies of transition metal carbides by core-level x-ray photoelectron spectroscopy free from Ar+ etching artefacts, Applied Surface Science. 436 (2018) 102–110.
https://doi.org/10.1016/j.apsusc.2017.11.264.

[38] Katrib A, Hemming F, Wehrer P, Hilaire L, Maire G, The multisurface strucure and catalytic properties of partially reduced WO3, WO2 and WC, Journal of Electron Spectroscopy and Related Phenomena. (1995) 195–200.

[39] H. Price, E. Lu¨pfert, D. Kearney, E. Zarza, G. Cohen, R. Gee, R. Mahoney, Advances in Parabolic Trough Solar Power Technology, Journal of Solar Energy Engineering. 124 (2002) 109–125. https://doi.org/10.1115/1.1467922.

[40] P. Bermel, J. Lee, J.D. Joannopoulos, I. Celanovic, M. Soljacie, SELECTIVE SOLAR ABSORBERS, Annual Rev Heat Transfer. 15 (2012) 231–254.
https://doi.org/10.1615/AnnualRevHeatTransfer.2012004119.

[41] C.E. Kennedy, Review of Mid- to High-Temperature Solar Selective Absorber Materials, 2002. https://doi.org/10.2172/15000706.

[42] S.V. Boriskina, H. Ghasemi, G. Chen, Plasmonic materials for energy: From physics to applications, Materials Today. 16 (2013) 375–386.
https://doi.org/10.1016/j.mattod.2013.09.003.

[43] A. Kuzma, M. Weis, M. Daricek, J. Uhrik, F. Horinek, M. Donoval, F. Uherek, D. Donoval, Plasmonic properties of Au-Ag nanoparticles: Distinctiveness of metal arrangements by optical study, Journal of Applied Physics. 115 (2014) 053517.
https://doi.org/10.1063/1.4864428.

[44] M. Coulibaly, G. Arrachart, A. Mesbah, X. Deschanels, From colloidal precursors to metal carbides nanocomposites MC (M=Ti, Zr, Hf and Si): Synthesis, characterization and optical spectral selectivity studies, Solar Energy Materials and Solar Cells. 143 (2015) 473–479. https://doi.org/10.1016/j.solmat.2015.07.039.

[45] A. Bousquet, F. Zoubian, J. Cellier, C. Taviot-Gueho, T. Sauvage, E. Tomasella, Structural and ellipsometric study on tailored optical properties of tantalum oxynitride films deposited by reactive sputtering, J. Phys. D: Appl. Phys. 47 (2014) 475201. https://doi.org/10.1088/0022-3727/47/47/475201.

[46] F. Zoubian, E. Tomasella, A. Bousquet, T. Sauvage, C. Eypert, Potential of TaOxNy thin films deposited by reactive sputtering as antireflective coatings: composition and optical properties, Advanced Materials Research. 324 (2011) 73–76. https://doi.org/10.4028/www.scientific.net/AMR.324.73.